HHS Public Access

Author manuscript

Nat Methods. Author manuscript; available in PMC 2024 June 01.

Published in final edited form as:

Nat Methods. 2023 December ; 20(12): 1920–1929. doi:10.1038/s41592-023-02065-w.

Adaptable, turn-on maturation (ATOM) fluorescent biosensors for multiplexed detection in cells

Harsimranjit Sekhon[1,2], **Jeung-Hoi Ha**[1,2], **Maria F. Presti**[1], **Spencer B. Procopio**[1], **Ava R. Jarvis**[1], **Paige O. Mirsky**[1], **Anna M. John**[1], **Stewart N. Loh**[✉,1]

[1]Department of Biochemistry and Molecular Biology, SUNY Upstate Medical University, Syracuse, NY, USA.

[2]These authors contributed equally: Harsimranjit Sekhon, Jeung-Hoi Ha.

Abstract

A grand challenge in biosensor design is to develop a single-molecule, fluorescent protein-based platform that can be easily adapted to recognize targets of choice. Here, we created a family of adaptable, turn-on maturation (ATOM) biosensors consisting of a monobody (circularly permuted at one of two positions) or a nanobody (circularly permuted at one of three positions) inserted into a fluorescent protein at one of three surface loops. Multiplexed imaging of live human cells coexpressing cyan, yellow and red ATOM sensors detected biosensor targets that were specifically localized to various subcellular compartments. Fluorescence activation involved ligand-dependent chromophore maturation with turn-on ratios of up to 62-fold in cells and 100-fold in vitro. Endoplasmic reticulum- and mitochondria-localized ATOM sensors detected ligands that were targeted to those organelles. The ATOM design was validated with three monobodies and one nanobody inserted into distinct fluorescent proteins, suggesting that customized ATOM sensors can be generated quickly.

Single-molecule, fluorescent protein-based biosensors (FPBs) are transforming the study of biochemical processes in cells and organisms. These proteins typically consist of one or more fluorescent proteins (FPs) fused to a receptor protein that confers specificity. Turnover-

✉**Correspondence and requests for materials** should be addressed to Stewart N. Loh. lohs@upstate.edu.

Author contributions

J.-H.H., H.S. and S.N.L. conceived and designed the study. H.S. validated the ATOM biosensors in mammalian cells. J.-H.H. compared ATOM to relating biosensors. H.S. and J.-H.H. performed all cloning. A.R.J., M.F.P., S.B.P., P.O.M. and S.N.L. purified and evaluated ATOM performance in vitro. H.S., J.-H.H. and S.N.L. wrote the paper, with contributions from all authors including A.M.J.

Online content

Any methods, additional references, Nature Portfolio reporting summaries, source data, extended data, supplementary information, acknowledgements, peer review information; details of author contributions and competing interests; and statements of data and code availability are available at https://doi.org/10.1038/s41592-023-02065-w.

Competing interests

The authors declare no competing interests.

Reporting summary

Further information on research design is available in the Nature Portfolio Reporting Summary linked to this article.

Extended data is available for this paper at https://doi.org/10.1038/s41592-023-02065-w.

Supplementary information The online version contains supplementary material available at https://doi.org/10.1038/s41592-023-02065-w.

based FPBs are constitutively fluorescent and report on analyte binding by becoming stabilized toward degradation, causing new sensor molecules to accumulate in the cell. A second class undergoes a conformational change on binding, producing a ratiometric fluorescence change (via Forster resonance energy transfer) or an increase in fluorescence intensity. We refer to the latter class as turn-on sensors.

Turn-on FPBs possess several qualities have made them among the most desirable sensor type in biology. First, their full genetic encoding allows them to be readily introduced into cells and used in many organisms. Second, they require no exogenous pathways or reagents for operation. Last, their fluorescence output modes make them useful for applications that demand quantification of ligand concentration as well as high sensitivity. Ratiometric signal establishes a response that is theoretically independent of sensor concentration and therefore consistent from cell to cell, and fluorescence turn-on provides high sensitivity (at the expense of precise quantification).

Perhaps the most influential example of a turn-on FPB is the genetically encoded calcium indicator (GECI) family of calcium sensors[1-3]. The output domain of GECIs is an FP that has generally been circularly permuted with its new amino and carboxy termini positioned in a β-strand that packs against the chromophore. The resulting structural defect allows the chromophore to mature but in a protonated state (presumably due to its increased solvent accessibility) that is consequently nonfluorescent or has a decreased fluorescence lifetime[4]. The recognition domain consists of calmodulin (CaM) and one of its cognate binding peptides (for example, ckkap[5,6] or RS20 (refs. 7,8)) fused to each terminus of the permuted FP. On binding Ca^{2+}, CaM associates with the peptide, closing around the permutation site and permitting the chromophore to deprotonate. By virtue of their strong and reversible fluorescence turn-on and rapid kinetics, GECIs have revolutionized the study of calcium signaling in cells. This sensing mechanism, however, has proved difficult to translate to recognition domains other than CaM. While successful examples exist[3], each sensor was the result of a new protein engineering effort whose outcome was far from guaranteed.

A major task facing inventors of FPBs is thus to create a protein switch that can be readily modified to sense new targets as they arise. An intuitive approach for doing so is to fuse an adaptable, antibody-like protein to an FP such that ligand binding activates fluorescence. Several engineered binding scaffolds[9] are available for this purpose, including monobodies (MBs)[10], nanobodies (NBs)[11,12], DARPins[13,14], affibodies[15] and de novo designed helical bundles[16,17]. These domains are advantageous because they are small (less than 15 kDa) and amenable to affinity maturation by in vitro and in vivo methods. Unlike CaM, however, they do not appreciably change conformation on binding. It therefore remains a formidable challenge to discover mechanisms by which ligand binding to the recognition domain translates to an increase in fluorescence of the FP domain.

Here, we created a family of adaptable turn-on maturation (ATOM) FPBs that are genetically encoded and can be easily modified to recognize a variety of ligands. We took advantage of a serendipitous observation from our earlier study in which we inserted a circularly permuted FK506-binding protein into the loop connecting strands β10 and β11 of a yellow FP (YFP) variant (YFP contains 11 β-strands)[18]. The YFP had itself been

circularly permuted between strands β9 and β10. The resulting fusion protein exhibited a 35-fold turn-on of yellow fluorescence on addition of FK506 or its analog rapamycin. We hypothesized that inserting a circularly permuted MB or NB between strands β10 and β11 of circularly permuted YFP, and possibly between other strands as well, would produce the same turn-on effect on binding the ligand to which the MB or NB was raised. We further surmised that sensors for new targets could be generated by swapping out one MB or NB for another, and that this mechanism might be transferrable to other colors and lineages of the FP.

We report the generation of cyan (c-ATOM), yellow (y-ATOM) and red (r-ATOM) biosensors incorporating MB domains that recognize the human proteins hRAS, c-Abl Src homology 2 (SH2) domain and WD repeat-containing protein 5 (WDR5), and a y-ATOM biosensor incorporating a NB domain that recognizes mCherry (mCh). The ATOM sensors displayed up to a 62-fold fluorescence turn-on in response to binding their cognate ligands in cells and more than 100-fold change in vitro. These sensors were created by inserting previously developed MBs and NBs into mTurquoise and YFP from *Aequorea victoria* and mTagRFP from *Entacmaea quadricolor*, at three different loops within the FPs. Unlike simple reporter molecules whose fluorescence is unchanged in bound and free states, ATOM sensors turn on because of binding. We demonstrated this capability in live and fixed human cells by detecting hRAS, SH2 and WDR5 proteins that were localized to the plasma membrane, cytoplasm and nucleus (respectively) in the same cells, using multiplexed three-color imaging and sensing endoplasmic reticulum (ER)- and mitochondria-resident SH2 protein using biosensor and SH2 that were targeted to those organelles.

ATOM sensors turn on by a new mechanism in which binding of the ligand to the MB or NB domain induces the FP chromophore to cyclize and mature. This differentiates ATOM from GECI as well as turnover-based sensors. This work defines a method for the high-probability discovery of additional ATOM sensors by fusing new MBs (circularly permuted at one of two locations) or new NBs (circularly permuted at one of three locations) into one of three surface loops in the FP. These six- or nine-member libraries can be rapidly screened in cells for the biosensor that yields the brightest turn-on in response to the coexpressed ligand.

Results

Biosensor design and optimization

The sensor input domains consisted of either MBs that had been previously engineered to recognize SH2 (ref. 19), WDR5 (ref. 20) and hRAS[21], or a NB that had been previously evolved to recognize mCh[22]. To make the distance between their amino and carboxy termini close enough to be compatible for insertion into surface turns of the FPs, we circularly permuted the MBs at one of two loops (MB1 and MB2) and the NB at one of four loops (NB1–NB4) that connect the β-strands of their β-sandwich scaffolds (Fig. 1a). These loops were chosen because they lie on the side of the proteins opposite to the ligand binding interface. The permuted binding domains are designated by their permutation site superscripted by the ligand that their parental proteins recognized (for example, $MB1^{WDR5}$, $NB2^{mCh}$ and so on).

ATOM sensors were then created by inserting a circularly permuted binding domain into a surface loop of an FP output domain. For initial biosensor development, we chose to insert MB1 or MB2 into a yellow variant of Clover FP (YFP) that had been circularly permuted between strands β9 and β10 of the 11-stranded β-barrel (Fig. 1b)[18,23]. We previously found that inserting a circularly permuted FK506-binding protein in the β10–β11 loop (FP3 in Fig. 1b) of the above YFP construct resulted in ligand-dependent turn-on, with the proposed mechanism shown schematically in Fig. 1c (ref. 18). For the present study, we inserted MB1 or MB2 into FP3 and explored two other FP loops as well: β7–β8 (FP1) and β8–β9 (FP2). The domain arrangements of ATOM sensors used in this study are shown in Table 1.

We screened the library of the MB-based y-ATOM biosensors in human cells to determine which combinations of MB permutation site and FP fusion site displayed the greatest fluorescence turn-on in the presence of ligand. For each ligand, there were six possible y-ATOM biosensors; we tested 15 of the 18 possible combinations for all three ligands (Fig. 1d and Supplementary Figs. 1-3). Human embryonic kidney 293T (HEK 293T) cells were cotransfected with one plasmid encoding the sensor and a second plasmid expressing the target ligand or one of the two noncognate ligands. The cells were then stained with an anti-green FP (GFP) antibody to verify biosensor expression, and the signal from each sensor was quantified by dividing the FP intensity by the antibody staining intensity. Most MB–FP combinations exhibited significant turn-on (Fig. 1d). The best-performing yellow sensor for each ligand (y-ATOM^{RAS}, y-ATOM^{SH2} and y-ATOM^{WDR5}) is shown in blue, orange and red boxes in Fig. 1d. Curiously, no single combination of YFP fusion location and MB permutation site proved to be the most successful. The YFP insertion sites in y-ATOM^{SH2}, y-ATOM^{RAS} and y-ATOM^{WDR5} were FP1, FP2 and FP3, respectively. MB1 gave the best results for y-ATOM^{WDR5} and y-ATOM^{SH2}, while MB2 worked optimally for y-ATOM^{RAS}.

Biosensor specificity in cells

Having determined the optimal combination of MB permutation and FP insertion for each y-ATOM sensor, we next evaluated their ability to discriminate between cognate and decoy ligands in human cells. HEK 293T cells were cotransfected with two plasmids: one harboring the *y-ATOM^{RAS}*, *y-ATOM^{SH2}* or *y-ATOM^{WDR5}* genes, and the other expressing hRAS, SH2, WDR5 or mCh. All three MB-based y-ATOM sensors demonstrated high turn-on for their cognate ligand (average of 25.3–27.0-fold, relative to the three negative control ligands; Fig. 2a). These turn-on ratios were consistent among three BRs (Table 1). BR in cellular experiments is defined as data obtained from independently transfected, freshly split cells on different days. BR in in vitro experiments is defined as data obtained from proteins purified from independent bacterial transformations and growths. We also tested y-ATOM^{SH2} performance in the human breast cancer cell line MDA-MB-231. MDA-MB-231 cells transfected with the y-ATOM^{SH2} plasmid showed similar activation (23-fold turn-on) when coexpressed with SH2 compared to mCh decoy ligand (Supplementary Fig. 4).

To establish whether the observed response resulted from fluorescence turn-on or decreased biosensor turnover, we transfected HEK 293T cells with y-ATOM sensors and ligands

as above, fixed them after 48 h and then stained the cells with an anti-GFP antibody conjugated with the red fluorescent dye Alexa594. Red fluorescence remained constant in cells expressing hRAS, SH2 and WDR5 (Extended Data Fig. 1), indicating that biosensor levels were similar in the presence of target ligand and decoy ligands. Turn-on in cells was therefore likely due to increased brightness of the sensor proteins. Extended Data Fig. 1 also demonstrates that the biosensors functioned in fixed cells as well as live cells.

Biophysical characterization of sensors

To gain further insight into mechanism and to determine binding affinities and kinetics, we expressed y-ATOM^{RAS}, y-ATOM^{SH2} and y-ATOM^{WDR5} in *Escherichia coli* at 37°C and purified the proteins using nickel-NTA chromatography. As anticipated, the sensors were mostly nonfluorescent (Fig. 3a). This was due to the absence of the YFP chromophore, which could be identified by an absorbance peak at 514 nm. There was no evidence of mature (but protonated) chromophore as this species absorbs near 400 nm (refs. 2,24). After the ligands were added, the 514 nm absorbance peaks appeared as did the expected fluorescence peak at 530 nm (Fig. 3a).

Fitting the time-dependent increases in fluorescence to single exponential functions revealed similar turn-on rates for y-ATOM^{WDR5} (k_{on} = 0.49 ± 0.12 h^{-1}) and y-ATOM^{SH2} (k_{on} = 0.38 ± 0.023 h^{-1}) at 37 °C (Fig. 3b and Table 1). These values are somewhat slower than the maturation rate of Clover FP (1.9 h^{-1})[25], although the maturation rate of the circularly permuted, yellow variant (Tyr203) of Clover that we used here has not been determined. Nevertheless, the data indicate that the k_{on} rate may be partially limited by a binding-induced conformational change step that preceded the chromophore maturation reaction. This scenario was almost certainly present for y-ATOM^{RAS}, which turned on roughly fourfold more slowly (k_{on} = 0.094 ± 0.0096 h^{-1}) than y-ATOM^{WDR5} and y-ATOM^{SH2}.

The fluorescence turn-on ratios of the y-ATOM sensors were calculated by dividing the fluorescence at the longest time point by the fluorescence at time zero, from the data in Fig. 3b. Turn-on ratios were more than 100-fold (y-ATOM^{RAS}), 4.9-fold (y-ATOM^{WDR5}) and 8.3-fold (y-ATOM^{SH2}) (Table 1). It is likely that the lower values observed for y-ATOM^{WDR5} and y-ATOM^{SH2} in vitro compared to in cells (22–24-fold; Fig. 2) were due to ligand-independent turn-on that occurred during the time of protein purification (roughly 3 h at room temperature). At this lower temperature, we observed slow chromophore maturation in the absence of ligands, presumably because the MB and/or FP domains were more stable than at 37°C. y-ATOM^{RAS} did not mature appreciably during purification, most likely because its intrinsic turn-on rate was roughly fourfold slower than those of y-ATOM^{WDR5} and y-ATOM^{SH2}.

Turn-on of y-ATOM^{WDR5} and y-ATOM^{RAS} was almost completely dependent on their respective ligands, but y-ATOM^{SH2} showed a minor increase in fluorescence in the presence of the negative control ligands, indicating a nonspecific activation process (Fig. 3b). To test for reversibility, we added excess competitor (MB1^{WDR5}) to the complex of y-ATOM^{WDR5} and WDR5. No decrease in fluorescence was observed, indicating that activation was irreversible (Supplementary Fig. 5). This result is consistent with a chromophore maturation mechanism.

We determined biosensor binding affinities by monitoring the increase in YFP fluorescence as a function of ligand concentration after incubation at 37 °C. Fitted dissociation constants (K_d) were 18.8 ± 5.2 nM (y-ATOM^{WDR5}), 1.62 ± 0.21 μM (y-ATOM^{SH2}) and 3.96 ± 0.29 μM (y-ATOM^{RAS}) (Fig. 3c and Table 1). These K_d values are higher than those of the parental (noncircularly permuted) MBs by factors of 3.8 (WDR5)[20], 74 (SH2)[19] and 240 (hRAS)[21]. It is likely the loss of affinity was due to a combination of circular permutation, coupling of ligand binding energy to conformational changes in the MB and FP domains, and possible steric effects of fusion to the FP protein.

Multiplexed cellular imaging using three-color ATOM sensors

We next designed ATOM sensors of two additional colors, cyan and red. mTurquoise differs from Clover by only seven residues, so we created the cyan sensor c-ATOM^{RAS} by circularly permuting mTurquoise at the same position we did for Clover and then inserting MB2^{RAS} into the same loop (FP2) that gave the best results for y-ATOM^{RAS}. We turned to the red FP scaffold mTagRFP to generate r-ATOM^{WDR5}. In addition, we used the unmodified mTagRFP sequence to determine whether ATOM sensors could be created without first circularly permuting the FP. Because of this difference, and because mTagRFP and Clover have very low sequence identity and possess different biophysical and photophysical properties, we repeated the optimization process by fusing MB1^{WDR5} into the three surface loops of mTagRFP that corresponded to those shown in Fig. 1b. Each construct was then cotransfected with WDR5 or SH2 expressing plasmids to quantify signal and background, respectively. The insertion point that yielded the highest turn-on normalized by total sensor expression was FP3, the same location that produced the greatest turn-on for y-ATOM^{WDR5} (Supplementary Fig. 6).

Specificity of the three-colored sensors was evaluated by cotrans-fecting HEK 293T cells with an equimolar mixture of r-ATOM^{WDR5}, c-ATOM^{RAS} and y-ATOM^{SH2} encoding plasmids and a fourth plasmid expressing WDR5, hRAS or SH2. WDR5, hRAS and SH2 localize primarily to the nucleus[26], the cytosolic face of the plasma membrane[21] and cytoplasm[27], respectively. We therefore fused a nuclear localization signal to r-ATOM^{WDR5} and a nuclear export signal (NES) to c-ATOM^{RAS}. The purpose of the NES was to reduce background signal coming from the small amount of ligand and sensor that entered the nucleus due to inefficient ribosome skipping of the polycistronic expression vector that encoded for the three ligands (vide infra). This occurred with all sensors, but even weak nuclear fluorescence can obscure visualization of plasma membrane proteins[28]. y-ATOM^{SH2} was not tagged with an NES or nuclear localization signal. As expected, we observed significant levels of only red fluorescence with WDR5 ligand (23-fold turn-on), only yellow fluorescence with SH2 ligand (22-fold turn-on) and only cyan fluorescence with hRAS ligand (22-fold turn-on) (Extended Data Fig. 2 and Table 1).

We next asked whether the red, cyan and yellow ATOM sensors could detect all three targets in the same cell, at their proper locations, in a multiplexed experiment. The three-color biosensor plasmid mix was cotransfected with fourth plasmid harboring *hRAS, SH2* and *WDR5* genes separated by the P2A ribosome skipping sequence. All three biosensors showed robust activation when cotransfected with the plasmid expressing the ligands (Fig.

4a, top and middle rows). Quantification revealed turn-on ratios of 38-fold (hRAS), 29-fold (SH2) and tenfold (WDR5) (Fig. 4b). Tracing a line through a single cell indicated sharp boundaries between nuclear, cytoplasmic and plasma membrane compartments and confirmed the expected localizations of WDR5, SH2 and hRAS, respectively (Fig. 4c).

The above results demonstrate that both *A. victoria* and *E. quadricolor* FPs can serve as output domains for the ATOM sensor mechanism. The *A. victoria* lineage covers blue to yellow FPs, and the *E. quadricolor* lineage extends emission from orange to far-red. The ATOM family of sensors therefore has the potential to span most of the visible spectrum, potentially allowing the detection of four or more colors in the same cell.

Detection of proteins in mitochondria and ER

Mitochondrial matrix and ER lumen can be challenging environments for protein-based biosensors, as the molecules must unfold and refold as they are translocated across the membranes, and the oxidative conditions in the ER can interfere with function of some FPs[29]. To establish whether ATOM sensors could be used for detecting targets in mitochondria and ER, we tagged y-ATOM^{SH2} and SH2 with peptides that directed them to those compartments. HeLa cells were cotransfected with a plasmid expressing ER-localized biosensor and a second plasmid encoding ER-localized SH2, mitochondrial matrix (mito)-localized SH2 or untagged SH2 (which expresses in the cytoplasm, Fig. 4). The ER-localized biosensor exhibited very little fluorescence in cells expressing mito-localized SH2 and untagged SH2 (Fig. 5a), and strong fluorescence in cells expressing ER-localized SH2. Similarly, cells transfected with mito-localized biosensor were mostly dark in the cells expressing ER-localized SH2 and untagged SH2 and were bright in cells expressing mito-localized SH2 (Fig. 5a). Quantification found turn-on ratios of 11–13-fold for ER-localized biosensors and/or ligands, and 15–19-fold for mito-localized biosensors and/or ligands, relative to the negative controls (Fig. 5c).

Confocal images confirmed that the biosensors were detecting their targets in the correct organelles, tracing the netlike pattern of the ER and the tubular structure of mitochondria (Fig. 5b). These results demonstrate that ATOM biosensors remained functional after translocation into the ER and mitochondria. Of note, the relatively slow k_{on} rate is advantageous for this application. If that rate were fast, the sensors may become activated in the cytoplasm if their targets are cytosolic and remain fluorescent after transport into ER and/or mitochondria due to the matured chromophore, causing nonspecific background in those organelles. Figure 5a demonstrates that this false positive mechanism does not occur appreciably with y-ATOM^{SH2}.

Detection of endogenous protein

A demanding task for a biosensor is to detect cellular proteins expressed at endogenous levels. An efficient turn-on mechanism is critical for this purpose, as target concentrations tend to be low and constitutively fluorescent reporters typically produce high background signal that obscures differentiation of bound versus free states. To test for endogenous detection, we transfected HEK 293T cells with a single plasmid encoding either y-ATOM^{WDR5} or a negative control (y-ATOM^{WDR5} with the R80A mutation in the MB1^{WDR5}

domain) that does not bind WDR5 (ref. 20). Staining with anti-GFP antibody established that total cellular expression of wild-type and R80A y-ATOM^{WDR5} was equal, that the biosensors expressed in both cytoplasm and nucleus and that most biosensor molecules were in the cytoplasm (Extended Data Fig. 3). Cells expressing y-ATOM^{WDR5} showed the same nuclear-localized yellow fluorescence observed in Fig. 4. As expected, biosensor activation (3.1-fold, relative to the R80A negative control) was less than that observed with overexpressed WDR5, but it was still significant and readily visualized. Cells expressing the R80A mutant sensor did not exhibit nuclear yellow fluorescence, indicating that turn-on of the wild-type sensor was WDR5-specific. We obtained similar results using COS-7 cells, verifying that the biosensor performed well in two cell lines (Supplementary Fig. 7). These data together establish that y-ATOM^{WDR5} was expressed throughout the cells in a dark state—turning on only in the presence of target ligand—and demonstrate its ability to detect endogenous WDR5 and determine that it localized to the nucleus.

NB-based ATOMs

We next asked whether ATOM biosensors could function with recognition domains other than MBs. We applied the same design approach using an mCh-binding NB. Slightly larger than MBs, NBs contain four loops that can serve as circular permutation/FP insertion sites (Fig. 1b). We made 12 y-ATOM^{mCh} variants by inserting NB1^{mCh}–NB4^{mCh} into FP1–FP3 of YFP and screened them in HEK 293T cells as described above. To remove optical crosstalk and fluorescence resonance energy transfer with biosensors, all experiments using mCh ligand used the Y70A mutant that removes a chromophore residue and renders mCh nonfluorescent. The NB library performed consistently better than the MB library, with NB1^{mCh}–NB3^{mCh} showing significant activation at almost all FP insertion sites (Fig. 1e and Supplementary Fig. 8). NB1^{mCh}–FP2 and NB1^{mCh}–FP3 were tied for the highest turn-on ratio and we chose NB1^{mCh}/FP2 for further testing (hereafter named y-ATOM^{mCh}). The NB4^{mCh} sensors were dimmer and less responsive than NB1^{mCh}–NB3^{mCh} sensors, leading us to conclude that the NB4 permutant was nonviable for ATOM.

Like the MB-based ATOMs, activation of y-ATOM^{mCh} in cells was specific to its cognate ligand in HEK 293T (Fig. 2) and MDA-MB-231 cells (Supplementary Fig. 4). The turn-on ratio of y-ATOM^{mCh} (62-fold relative to the three decoy ligands) was more than twofold higher than that of the MB ATOMs (Table 1). We verified that y-ATOM^{mCh} was activated by the chromophore maturation mechanism in cells by antibody staining experiments (Extended Data Fig. 1). In vitro characterization of purified protein found that y-ATOM^{mCh} turned on with similar kinetics as the MB ATOMs and bound Y70A mCh with a K_d of 390 nM (Fig. 3 and Table 1). NBs and MBs adopt similar β-sandwich structures (Fig. 1a) but are less than 16% identical in sequence. Thus, the ATOM mechanism is compatible with recognition domains of the Ig-fold family, and potentially with other folds as well, and does not depend on a specific amino acid sequence of either the binding or FP domains.

Comparison with turnover-based biosensors

Several groups have developed turnover-based FPBs by joining unstable NB[30,31] and other binding domains[32,33] to FPs. The OFF state of these sensors is their physical absence from the cell due to constant removal by the ubiquitin-proteasome pathway. Ligand binding

stabilizes the sensor toward degradation, allowing the bound sensor to accumulate by synthesis of new molecules. One potential difference between ATOM and turnover-based FPBs is that the latter may be challenged to operate in cellular compartments that lack protein synthesis and/or degradation machinery. To explore this distinction, we repeated the mitochondrial and ER targeting experiments of Fig. 5 using the turnover-based sensor family called NIR-Fb[30]. These sensors consist of a biliverdin-dependent, near-infrared, cyanobacteriochrome FP inserted into a NB. We chose the GFP–Clover-binding version (NIR-Fb_{GFP}) for these studies.

We attached subcellular localization tags to NIR-Fb_{GFP} and Clover as described above and measured activation when sensor and Clover were directed to the same compartment (cytoplasm, mitochondria or ER) compared to when the ligands were directed to the two different compartments. Cytoplasmic NIR-Fb_{GFP} displayed a 21.7-fold turn-on in HEK 293T cells coexpressing cytoplasmic Clover compared to those coexpressing cytoplasmic decoy (Supplementary Table 1). Treating cells with the proteasome inhibitor bortezomib (10 μM, 12–16 h) reduced NIR-Fb_{GFP} activation by more than tenfold. These results reproduced those of Oliinyk et al.[30] in our system.

While cytoplasmic NIR-Fb_{GFP} responded in the expected manner to cytoplasmic ligand, it was also activated by mito-localized Clover (Extended Data Fig. 4 and Supplementary Table 2). This likely reflected binding of NIR-Fb_{GFP} to Clover in the cytoplasm, before Clover was translocated into mitochondria. Similarly, mito-localized NIR-Fb_{GFP} was activated not only by mito-localized Clover but also by cytoplasmic ligand to a greater extent (Extended Data Fig. 4 and Supplementary Table 2). Robust turn-on by cytoplasmic Clover, which does not enter mitochondria, suggests that mito-localized NIR-Fb_{GFP} became activated in the cytoplasm, before the biosensor could be translocated into mitochondria. ER-localized NIR-Fb_{GFP} was dimmer than when it was localized to mitochondria and cytoplasm, and it failed to become activated by Clover that was localized to any of the three compartments (Extended Data Fig. 4 and Supplementary Table 2). Imaging the cells in the green channel found the greatest Clover expression in the ER (Extended Data Fig. 4), ruling out a lack of ER-resident ligand as the cause of nonactivation. Instead, lack of turn-on may have been due to insufficient biliverdin in the ER.

By contrast, parallel experiments determined that y-$ATOM^{SH2}$ was activated only when the biosensor and its target were localized to the same organelle, and that it functioned equally well in ER, cytoplasm and mitochondria (Supplementary Table 2). Turn-on of cytoplasmic y-$ATOM^{SH2}$ (22.3-fold) and cytoplasmic y-$ATOM^{mCh}$ (73.7-fold) by their respective cytoplasmic ligands was not affected by bortezomib treatment (Supplementary Table 1). These results further corroborate that ATOM sensors do not operate by the turnover mechanism.

Discussion

The ATOM biosensors combine a fluorescent reporter protein with a MB or NB input domain to detect binding of target ligands with high specificity. Because they are ON and OFF switches, multiple ATOM sensors of different colors can be simultaneously

overexpressed in cells, where they become fluorescent only when encountering their ligands in their specific cellular locations. This property was demonstrated by detecting three separate proteins in a single mammalian cell, in locales including plasma membrane, cytoplasm, nucleus, ER and mitochondria. This result would not have been feasible using simple, overexpressed reporter proteins, for example, NBs or other binding domains fused at one of their termini to GFP.

Although the activation mechanisms of ATOM and turnover-based FPBs are fundamentally different, they both achieve modularity by employing an adaptable binding domain that has been engineered to be unstable. It is unclear why ATOM sensors are not degraded by the ubiquitin–proteasome system in the absence of ligands, as are the NIR-Fb class, despite y-ATOM^{mCh} and NIR-Fb$_{GFP}$ possessing NB binding domains whose parental sequences are 63% identical and 77% similar. This finding indicates that the binding domains of ATOM sensors may be structured and stable enough to resist degradation but are in a conformation that distorts the FP structure at the points of insertion, preventing chromophore maturation.

In the above respect, ATOM sensors and GECIs both function by binding-induced conformational change of the binding domain being transmitted to the FP domain. Their mechanisms are distinct in two ways, however, making each FPB befitted to different tasks. First, the ATOM sensing mechanism involves irreversible chromophore maturation, while that of GECIs entails reversible deprotonation of the chromophore. GECIs therefore excel at reporting on rapid (millisecond scale) fluctuations in analyte concentration, whereas ATOM sensors are best suited to detect intracellular targets that may be present at low abundance and when signal accumulation is desired or acceptable. The chromophore maturation mechanism lends itself to high sensitivity, as unmature chromophores are completely dark and thus produce large signal-to-noise ratios on maturation. The second difference is that ATOM sensors are designed from the ground up to be adaptable by virtue of the MB and NB domains. MBs can be evolved in vitro to recognize new ligands, and NBs (being derived from antibodies) can be generated efficiently from animals. For either protein, there is no requirement for a binding-induced conformational change. By contrast, each GECI-type biosensor is constructed using a unique domain that typically dimerizes on ligand binding (for example, CaM/RS20 peptide), and this type of conformational change is not readily transferable to other targets.

Because we observed ligand-assisted chromophore maturation with multiple combinations of MB permutation site, NB permutation site and FP insertion loop, this phenomenon is not strictly dependent on a particular amino acid sequence or structure that comprises the interface between the two proteins. We previously showed that binding-induced stabilization of a circularly permuted FK506-binding protein stabilized the FP into which it was inserted by a mechanism known as loop-closure entropy[18], and that loop-closure entropy can be a particularly efficient means to effect allosteric communication between domains[34]. If the loop-closure entropy switching mechanism is operational in the present case, it is reasonable to speculate that new families of ATOM sensors may be created using altogether different binding domains that are circularly permuted before insertion into the FP.

A potential caveat of ATOM technology is that some MBs or NBs may cause the sensor to express poorly or aggregate in cells. We did not encounter this problem in the present study, but the effects of sequence variability (which occurs in both the CDR-like loops and constant regions of MBs and/or NBs) on protein expression and solubility cannot be anticipated. Another consideration is the thermodynamic stability of the MB–NB domain. If too stable or too unstable, our model predicts the sensor would be always ON or always OFF regardless of ligand, respectively. The screening results (Fig. 1) suggest that MB1–MB2 and NB1–NB4 span the range of stabilities appropriate for activating the FP domains. In future ATOM sensors, if screening reveals the cells to be always bright or always dark (and expressing biosensor by antibody staining), this issue can be addressed by destabilizing or stabilizing the MB–NB domain using known mutations[35,36]. Priorities for expanding the versatility of the ATOM design include incorporating new binding scaffolds in addition to MBs and NBs, such as affibodies and DARPins, and decreasing the turn-on half-lives to their minimum values, that is, the maturation times of the parent FPs.

Although the ATOM sensing mechanism remains to be fully delineated, we showed that it worked with three out of three arbitrarily chosen MBs and one out of one arbitrarily chosen NB, as well as FPs from jellyfish and anemone lineages. This result indicates that ATOM sensors with different binding specificities and colors can be generated rapidly from new MBs and NBs, with a minimum of optimization. To do so, we recommend synthesizing the six-member gene MB library or the nine-member NB1–NB3 library described in Fig. 1, and screening by cotransfection as shown in Fig. 2. If our results are representative, at least one of the proteins will likely be a functioning ATOM sensor. This process stands in contrast to the large libraries and multiple iterations of screening and/or selection that are used when developing many other single-molecule fluorescent biosensors[37,38].

Methods

Gene construction

For bacterial expression, C-terminal 8×-His tagged biosensor genes were cloned into pET41 expression vector downstream of the T7 promoter using NdeI and/or XhoI restriction sites. The y-ATOM^{RAS} sensor expressed poorly in *E. coli*, so ribose-binding protein was fused to its N terminus to improve solubility and overall expression[39]. y-ATOM^{WDR5}, y-ATOM^{SH2} and y-ATOM^{mCh} did not contain ribose-binding protein fusions.

For mammalian cell expression, ATOM genes were cloned into the N1 vector (Clontech) under the cytomegalovirus promoter using AgeI/NotI restriction sites. The genes were then fused to the 3′-end of the maltose-binding protein gene using the EcoRI/AgeI sites. WDR5, SH2 and hRAS (G12V variant) proteins were constructed without any exogenous localization tags. The C-terminal CAAX farnesylation sequence was deleted from hRAS in all experiments except for the multiplexed three-color detection study (Fig. 4). For that last experiment, the r-ATOM^{WDR5} and c-ATOM^{RAS} proteins were tagged with a nuclear localization signal (MPKKKRKV) and NES (MNLVDLQKKLEELELDEQQG), respectively, at the N terminus of maltose-binding protein. The ER-localized y-ATOM^{SH2} sensor and ligand were tagged with the prolactin secretion signal (MNIKGSPWKGSLLLLLVSNLLLCQSV) at their N termini and the ER retention signal

(KDEL) at their C termini. The mitochondria-localized y-ATOM^{SH2} sensor and ligands were tagged with the COX4 signal peptide (MLSLRQSIRFFKPATRTLCSSRYLL) at their N termini. All genes were fully sequenced. Amino acid sequences of biosensors and ligands are provided in Supplementary Fig. 9. Primer sequences are included in Supplementary Table 1.

The following genes were obtained from Addgene: *mTagRFP-pBAD* (a gift from D. Chudakov, M. Davidson and D. Gadella; Addgene plasmid no. 54539; RRID:Addgene_54539), *Clover-pBAD* (a gift from M. Davidson; Addgene plasmid catalog no. 54575; RRID:Addgene_54575), *pET21-pelB-LaM-8* (a gift from M. Rout; Addgene plasmid catalog no. 172772; RRID:Addgene_172772) and *pmiRFP670nano3-NbGFP* and *pNbGFP-miRFP670nano3* (gifts from V. Verkhusha; Addgene plasmid catalog nos. 184686 and 184687; RID:Addgene_184686 and RRID:Addgene_184687).

In vitro equilibrium binding and kinetic experiments

ATOM sensors were expressed in *E. coli* BL21(DE3) cells and induced with 0.3 mM isopropyl β-D-thiogalactopyranoside for 3–4 h at 37 °C. WDR5, SH2, hRAS and mCh ligand proteins were expressed as above except cells were induced at 18 °C for 12–16 h. All sensor and ligand proteins except for SH2 were purified by nickel–nitrilotriacetate chromatography according to the manufacturer's instructions (Molecular Cloning Laboratories). SH2 did not have a His-tag and was purified using an SP Sepharose column as described[35]. Sensors were purified at room temperature and ligands at 4°C. On elution from the nickel–nitrilotriacetate columns, ATOM sensors were desalted into experimental buffer (20 mM Tris, pH 8.0, 0.15 M NaCl, 0.005% Tween 20) using DG10 columns (Bio-Rad) and experiments began immediately. Total purification time was roughly 3h.

Fluorescence kinetic experiments were performed by mixing 10–50 nM of biosensor with 10 μM of each ligand and transferring to a 37 °C bath at time zero. At the indicated times, 100 μl of samples was aliquoted onto a fully blackened 96-well plate (Corning Costar) and fluorescence spectra were recorded using a Molecular Devices i3x plate reader (475 nm excitation, 500–650 nm emission). To measure binding affinities, a solution of biosensor (10–50 nM) plus ligand (20 μM SH2 or hRAS, 10 μM mCh or 5 μM WDR5) was serially diluted twofold into solutions of biosensor only to generate the indicated ligand concentrations. Samples were incubated for 2–24 h at 37°C and fluorescence spectra were recorded as above.

Cell culture and transfection

HEK 293T (CRL-3216), COS-7 (CRL-1651), MDA-MB-231 (HTB-26) and HeLa (CCL-2) cells were purchased from ATCC and cultured at 37°C in DMEM containing 10% FBS and 1× penicillin–streptomycin. Cells were split into a 12-well plate containing round 15 mm glass coverslips 1 day before transfection at a confluency of 60–80%. HEK 293T and COS-7 cells were transfected using the calcium phosphate method as previously described[18,34]. MDA-MB-231 cells were transfected using Lipofectamine 3000 (Invitrogen) according to the manufacturer's protocol. HeLa cells were transfected using the TransIT-2020 reagent

(Mirus Bio) according to the manufacturer's protocol. After 36–48 h of expression, cells were washed and mounted on imaging media (DMEM, 25 mM HEPES, pH 7.0). All imaging was performed on live cells except the three-color multiplexed imaging experiments (Fig. 4), the antibody labeling experiments and data contained in Extended Data Fig. 4 and Supplementary Table 2, all of which used paraformaldehyde fixed cells. The ligand-to-biosensor plasmid ratio was one to five for the screening experiments in Fig. 1 to quantify weakly fluorescent biosensors; transfections for all other experiments contained equal ratios of ligand and biosensor plasmids.

Antibody staining

After 36–48 h of expression, the cells were fixed with 2.5% paraformaldehyde in PBS for 20 min, followed by three 5 min washes in 20 mM Tris (pH 7.5), 150 mM NaCl. Permeabilization and blocking was then performed by incubating the cells in blocking buffer (5% BSA, 0.25% Triton X-100 in 20 mM Tris, pH 7.5, 150 mM NaCl) for 30 min. The rabbit-anti-GFP-Alexa594 conjugate or rabbit-anti-RFP antibodies (Thermo Fisher Scientific, catalog nos. A21312 and R10367, respectively) were diluted 1:1,000 in blocking buffer, and the cells were labeled for 1 h at room temperature, followed by three 5 min washes with 20 mM Tris (pH 7.5), 150 mM NaCl. The anti-RFP antibodies were labeled with anti-rabbit-Alexa488 conjugate (Thermo Fisher, catalog no. XE353106) at 1:1,000 dilution in blocking buffer for 1 h at room temperature, followed by three 5 min washes with 20 mM Tris (pH 7.5), 150 mM NaCl. The coverslips were then mounted in 50% glycerol, 20 mM Tris (pH 8.5), 50 mM NaCl and sealed with nail polish.

Imaging

The images in Fig. 2, Extended Data Fig. 3 and Supplementary Fig. 4 were acquired on a Zeiss Axiovert 200 m inverted microscope with a ×10/0.3 Plan-Neofluor objective. Screening and antibody staining experiments (Fig. 1 and Supplementary Figs. 1-3, 6 and 8) employed a Zeiss Axioimager Z1 upright microscope with ×10/0.25 A-Plan objective. The images contained in Figs. 4 and 5, Extended Data Fig. 4 and Supplementary Table 2 were collected on a Leica SP8 inverted laser-scanning confocal microscope using 405 nm excitation for mTurqoise, 488 nm excitation for YFP, 552 nm excitation for mTagRFP and 638 nm excitation for NIR-Fb_{GFP}. Low-magnification confocal images were obtained using a ×20 dry objective with the pinhole opened to 5 Airy units, allowing imaging at a low laser power to avoid phototoxicity and bleaching. The high-magnification images were taken using a ×63 oil-immersion objective with pinhole closed to 1 Airy unit.

For each experiment, at least three fields containing at least 30 cells each were imaged, and all three fields were pooled for quantification of that sample. The images were quantified using Fiji[40]. Background was subtracted using the built-in plugin using 50 pixels as the sliding ball radius followed by subtracting the average intensity of three to five regions without cells, and no further processing was applied. The images displayed were contrast-adjusted using the positive control for visualization only, and the same contrast was applied to all images containing the same biosensor. No adjustment other than background correction was made for quantification. The intensity of each cell was measured by manually

drawing a region of interest around each cell and determining the average intensity using the Measure Particles plugin.

Reproducibility and statistics

All experiments described in this study were performed a minimum of three times without sample size estimation for power. The in-cell experiments consisted of more than three BRs with new cells freshly split and transfected on different days. For in vitro experiments, sensor proteins were purified at least twice for independent BR, with three technical repeats of each preparation. The statistical significance, where stated, was determined by a two-sided *t*-test with unequal variance using GraphPad Prism (v.10.0). The investigators were not blinded during the experiments or analysis.

Extended Data

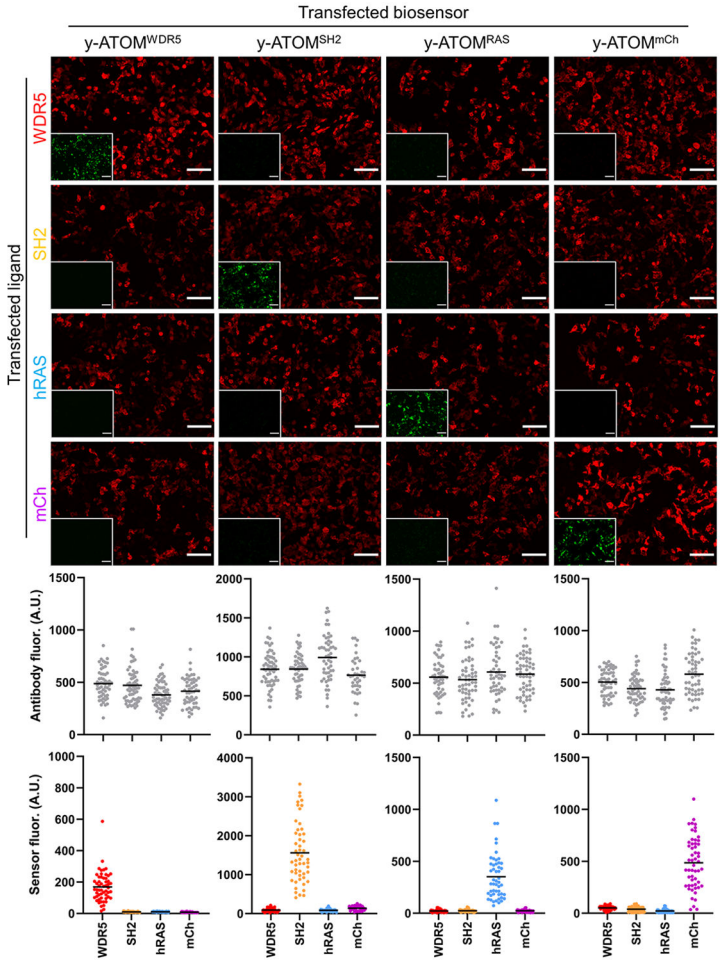

Extended Data Fig. 1 |. Ligand-dependent ATOM turn-on in cells is not due to increased biosensor levels.

HEK 293T cells were co-transfected with one plasmid encoding y-ATOM^{WDR5}, y-ATOM^{SH2}, y-ATOM^{RAS}, or y-ATOM^{mCh} and a second plasmid expressing WDR5, SH2, hRAS, or mCh. After 48 h, cells were fixed, stained with an anti-GFP antibody conjugated

with Alexa594, and imaged in the red channel (antibody; data depicted as gray points) and yellow channel (biosensor; data depicted in indicated colors). Each data point represents a cell (50–100 per experiment). Scale bars are 200 μm. The results are representative of three BR. Number of cells, means, standard deviations, and *P* values obtained by a two-tailed *t*-test for all valid comparisons are included in Extended Data Table 1.

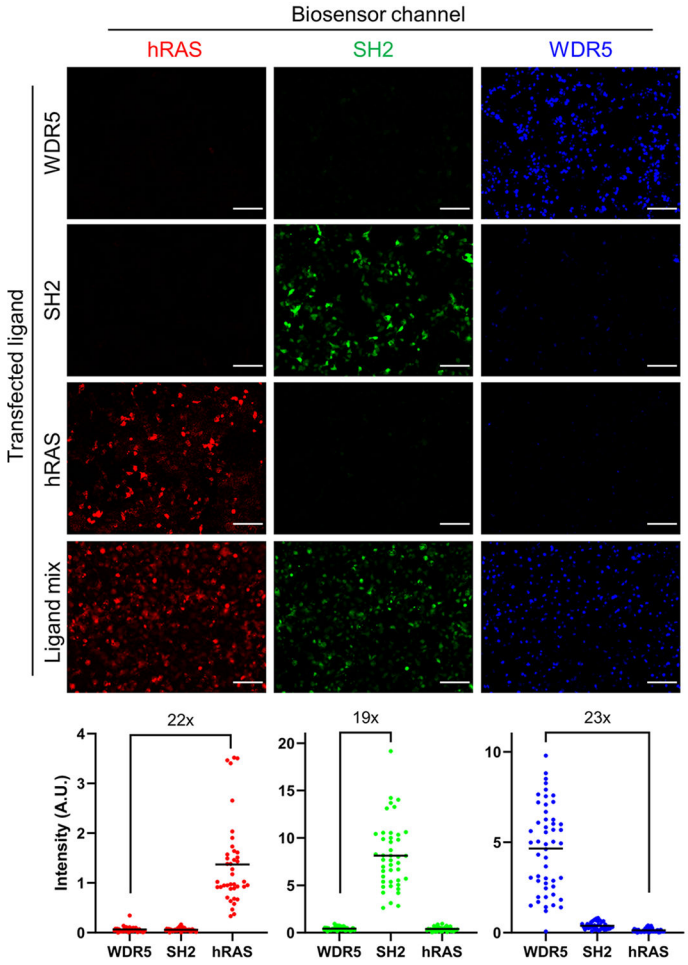

Extended Data Fig. 2 |. r-ATOM^{WDR5}, y-ATOM^{SH2}, and c-ATOM^{RAS}, co-expressed in the same cells, exhibit high turn-on values in the presence of their target ligands but not in the presence of noncognate ligands.

To match Fig. 4, the cyan channel (hRAS) is pseudocolored red, the yellow channel (SH2) is pseudocolored green, and the red channel (WDR5) is pseudocolored blue. HEK 293T cells were co-transfected with an equimolar mixture of three biosensor plasmids and a fourth plasmid encoding WDR5 (first row), SH2 (second row), and hRAS (third row). The fourth row shows the same experiment, but the fourth plasmid expressed all three ligands as described in the text. Scale bars are 200 μm. Turn-on ratios in each color channel (bottom plots) were calculated by dividing the average intensity of cells expressing the biosensor and its cognate ligand by the average of the intensities of cells expressing the same biosensor and the two negative control ligands. Each data point represents a cell (40–60 per experiment). $P < 10^{-4}$ for all comparisons shown. The results are representative of three BR. Number of

cells, means, standard deviations, and *P* values obtained by a two-tailed *t*-test for all valid comparisons are included in Extended Data Table 1.

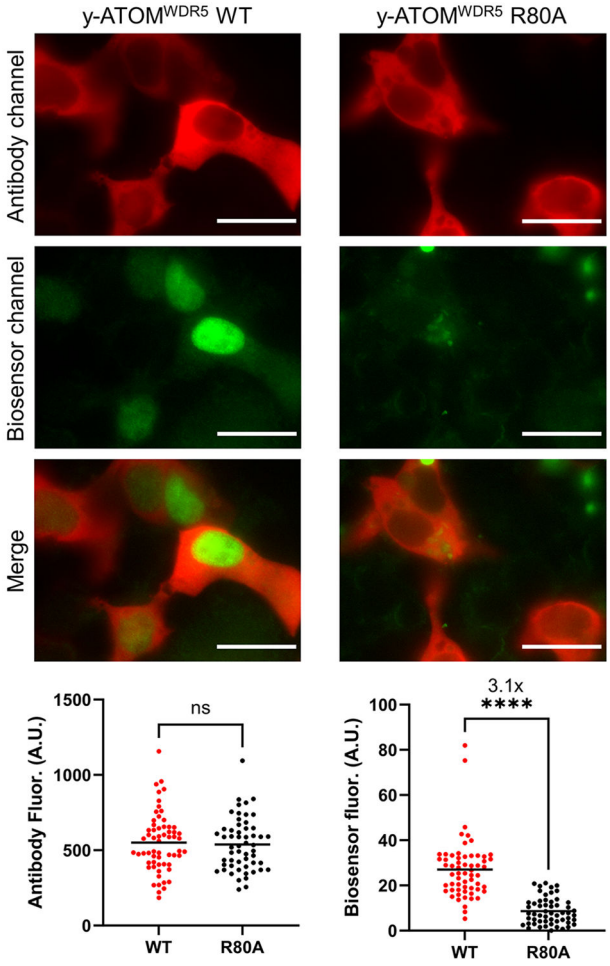

Extended Data Fig. 3 |. y-ATOM^{WDR5} detects endogenous WDR5 and identifies nuclear localization in HEK 293T cells.

Staining with anti-GFP antibody (red) indicated that WT and R80A mutant y-ATOM^{WDR5} were both expressed in cytoplasm and nucleus, with highest levels in the cytoplasm. Imaging in the yellow channel (pseudocolored green) showed the WT biosensor was activated in the nucleus but in the OFF state in the cytoplasm. R80A y-ATOM^{WDR5} was dark in both cytoplasm and nucleus. Scale bars are 20 μm. Each data point represents one cell (61 cells per experiment). ****, $P < 10^{-4}$; ns, not significant. Results are representative of 3 BR. Number of cells, means, standard deviations, and *P* values obtained by a two-tailed *t*-test for all valid comparisons are included in Extended Data Table 1.

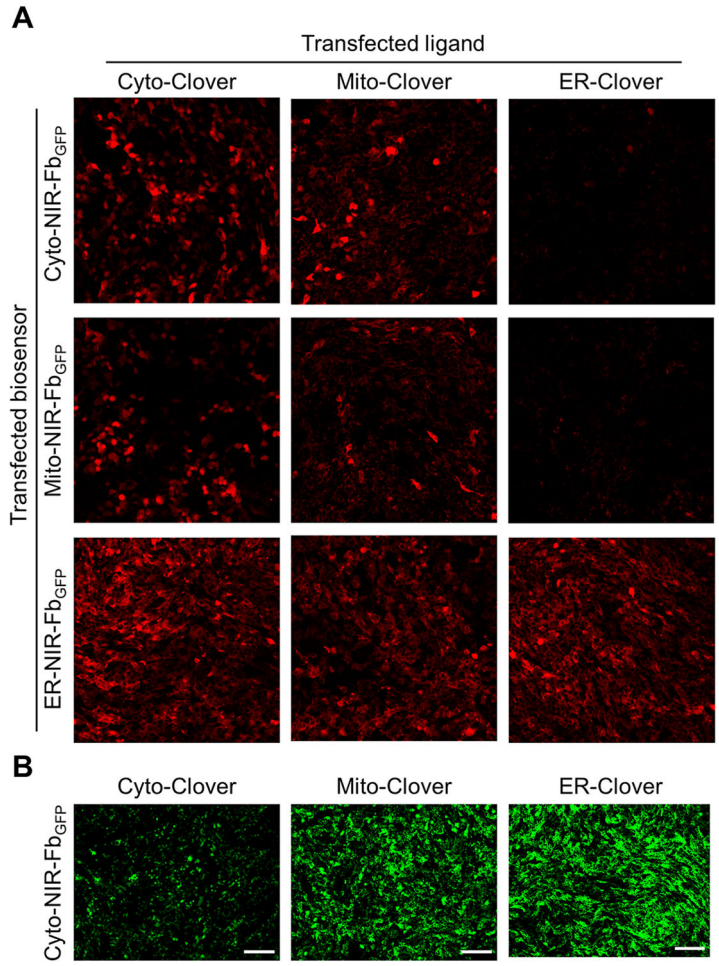

Extended Data Fig. 4 |. Performance of NIR-Fb$_{GFP}$ localized to cytoplasm, mitochondria, and ER of HEK 293T cells.

Cells were co-transfected with plasmids encoding NIR-Fb$_{GFP}$ and Clover (tagged with indicated localization sequences) and imaged in the far-red channel to quantify compartment-specific turn-on. **(b)** The same cells were imaged in the green channel to determine relative Clover expression. Scale bars are 200 μm. Results are representative of 3 BR.

Extended Data Table 1 |

Statistical values for cellular data shown in Figures

Figure	Condition	Average	Std. Dev.	n	p value
Fig.1D	MB1^{Ras}-FP1 + Ligand	1.291	0.517	54	2.9×10^{-8}
	MB1^{Ras}-FP1 − Ligand	1.909	0.536	51	
	MB1^{Ras}-FP2 + Ligand	0.176	0.07	53	2.2×10^{-18}
	MB1^{Ras}-FP2 − Ligand	0.322	0.071	53	
	MB1^{Ras}-FP3 + Ligand	0.073	0.032	49	1.3×10^{-6}
	MB1^{Ras}-FP3 − Ligand	0.048	0.012	54	

Figure	Condition	Average	Std. Dev.	n	p value
	$MB2^{Ras}$-FP1 + Ligand	1.624	0.625	52	2.0×10^{-6}
	$MB2^{Ras}$-FP1 − Ligand	1.134	0.322	53	
	$MB2^{Ras}$-FP2 + Ligand	0.588	0.495	44	4.2×10^{-9}
	$MB2^{Ras}$-FP2 − Ligand	0.097	0.049	43	
	$MB2^{Ras}$-FP3 + Ligand	0.173	0.121	43	6.0×10^{-5}
	$MB2^{Ras}$-FP3 − Ligand	0.091	0.034	36	
	$MB1^{SH2}$-FP1 + Ligand	1.620	0.956	37	1.4×10^{-7}
	$MB1^{SH2}$-FP1 − Ligand	0.700	0.26	56	
	$MB1^{SH2}$-FP2 + Ligand	0.212	0.139	47	3.7×10^{-5}
	$MB1^{SH2}$-FP2 − Ligand	0.121	0.045	59	
	$MB1^{SH2}$-FP3 + Ligand	0.047	0.02	52	1.4×10^{-2}
	$MB1^{SH2}$-FP3 − Ligand	0.038	0.012	45	
	$MB2^{SH2}$-FP1 + Ligand	0.531	0.306	48	4.4×10^{-3}
	$MB2^{SH2}$-FP1 − Ligand	0.390	0.135	48	
	$MB2^{SH2}$-FP2 + Ligand	0.070	0.031	48	1.6×10^{-2}
	$MB2^{SH2}$-FP2 − Ligand	0.083	0.020	50	
	$MB2^{SH2}$-FP3 + Ligand	0.066	0.024	51	$8.4 - 10^{-5}$
	$MB2^{SH2}$-FP3 − Ligand	0.050	0.014	50	
	$MB1^{WDR5}$-FP1 + Ligand	2.795	0.623	53	0.7
	$MB1^{WDR5}$-FP1 − Ligand	2.862	0.848	53	
	$MB1^{WDR5}$-FP2 + Ligand	0.235	0.09	41	1.4×10^{-10}
	$MB1^{WDR5}$FP2 − Ligand	0.121	0.044	44	
	$MB1^{WDR5}$-FP3 + Ligand	0.351	0.195	53	3.23×10^{-17}
	$MB1^{WDR5}$-FP3 − Ligand	0.071	0.017	41	
Fig. 1E	$NB1^{mCherry}$-FP1 + Ligand	5.249	3.006	48	1.3×10^{-19}
	$NB1^{mCherry}$-FP1 − Ligand	0.315	0.224	53	
	$NB1^{mCherry}$-FP2 + Ligand	5.102	2.668	51	1.7×10^{-23}
	$NB1^{mCherry}$-FP2 − Ligand	0.146	0.111	48	
	$NB1^{mCherry}$-FP3 + Ligand	2.015	1.184	47	2.8×10^{-19}
	$NB1^{mCherry}$-FP3 − Ligand	0.047	0.035	47	
	$NB2^{mCherry}$-FP1 + Ligand	6.180	3.912	45	0.14
	$NB2^{mCherry}$-FP1 − Ligand	5.028	3.686	51	
	$NB2^{mcherry}$-FP2 + Ligand	3.502	2.417	47	1.4×10^{-3}
	$NB2^{mCherry}$-FP2 − Ligand	2.131	1.561	48	
	$NB2^{mCherry}$-FP3 + Ligand	5.490	4.460	45	1.3×10^{-9}
	$NB2^{mCherry}$-FP3 − Ligand	0.941	0.736	48	
	$NB3^{mCherry}$-FP1 + Ligand	5.842	2.793	44	6.6×10^{-11}
	$NB3^{mCherry}$-FP1 − Ligand	1.955	2.008	43	
	$NB3^{mCherry}$-FP2 + Ligand	3.262	1.941	43	4.9×10^{-15}

Figure	Condition	Average	Std. Dev.	n	p value
	$NB3^{mCherry}$-FP2 − Ligand	0.416	0.248	43	
	$NB3^{mCherry}$-FP3 + Ligand	2.602	1.588	45	1.1×10^{-16}
	$NB3^{mcherry}$-FP3 − Ligand	0.142	0.094	41	
	$NB4^{mcherry}$-FP1 + Ligand	0.022	0.009	40	1.2×10^{-2}
	$NB4^{mCherry}$-FP1 − Ligand	0.028	0.013	48	
	$NB4^{mcherry}$-FP2 + Ligand	0.175	0.161	34	2.4×10^{-3}
	$NB4^{mCherry}$-FP2 − Ligand	0.083	0.063	42	
	$NB4^{mCherry}$-FP3 + Ligand	0.109	0.097	43	2.8×10^{-5}
	$NB4^{mCherry}$-FP3 − Ligand	0.042	0.016	35	
Fig. 2	y-$ATOM^{WDR5}$ + WDR5 Ligand	500.842	218.41	77	-
	y-$ATOM^{WDR5}$ + SH2 Ligand	17.441	17.124	69	6.7×10^{-42}
	y-$ATOM^{WDR5}$ + Ras Ligand	23.404	9.794	83	4.6×10^{-43}
	y-$ATOM^{WDR5}$ + mCherry Ligand	19.719	9.192	69	8.5×10^{-42}
	y-$ATOM^{SH2}$ + WDR5 Ligand	48.324	21.277	75	1.1×10^{-41}
	Y-$ATOM^{SH2}$ + SH2 Ligand	1136.444	520.665	81	-
	y-$ATOM^{SH2}$ + Ras Ligand	36.924	15.501	88	1.4×10^{-43}
	y-$ATOM^{SH2}$+ mCherry Ligand	43.664	13.537	82	1.1×10^{-42}
	y-$ATOM^{Ras}$ + WDR5 Ligand	58.435	22.591	78	1.2×10^{-42}
	y-$ATOM^{Ras}$ + SH2 Ligand	54.502	25.376	75	2.0×10^{-42}
	y-$ATOM^{Ras}$ + Ras Ligand	1474.977	651.868	78	-
	y-$ATOM^{Ras}$ + mCherrv Ligand	51.857	20.043	79	5.3×10^{-43}
	y-$ATOM^{mCherry}$ + WDR5 Ligand	23.172	10.111	73	4.6×10^{-44}
	Y-$ATOM^{mCherry}$ + SH2 Ligand	25.768	6.988	75	3.1×10^{-44}
	y-$ATOM^{mCherry}$ + Ras Ligand	21.108	6.941	76	1.6×10^{-44}
	y-$ATOM^{mCherry}$ + mCherry Ligand	1461.87	611.674	74	-
Fig.4	c-$ATOM^{Ras}$ + Ligand	1620.837	603.560	40	6.6×10^{-27}
	c-$ATOM^{Ras}$ − Ligand	68.580	27.119	41	
	y-$ATOM^{SH2}$ + Ligand	1362.753	715.109	40	7.6×10^{-18}
	y-$ATOM^{SH2}$ − Ligand	102.874	37.446	41	
	y-$ATOM^{WDR5}$ + Ligand	736.1143	320.735	40	2.1×10^{-19}
	y-$ATOM^{WDR5}$ − Ligand	124.372	45.182	41	
Fig. 5	ER-y-$ATOM^{SH2}$+ Cyto-SH2	1506.589	635.169	59	3.1×10^{-22}
	ER-y-$ATOM^{SH2}$+ ER-SH2	15876.090	9117.167	59	-
	ER-y-$ATOM^{SH2}$+ Mito-SH2	1202.914	477.642	53	1.7×10^{-22}
	Mito-y-$ATOM^{SH2}$+ Cyto-SH2	943.944	435.765	63	3.3×10^{-20}
	Mito -y-$ATOM^{SH2}$+ ER-SH2	758.138	478.202	52	5.7×10^{-20}
	Mito -y-$ATOM^{SH2}$+ Mito-SH2	14215.78	8578.717	53	-
Extended Data Fig. 1	Ab: y-$ATOM^{WDR5}$ + WDR5 Ligand	486.886	139.292	55	-
	Ab: y-$ATOM^{WDR5}$ + SH2 Ligand	471.002	170.046	62	0.58

Figure	Condition	Average	Std. Dev.	n	p value
	Ab: y-ATOM^{WDR5} + Ras Ligand	378.805	113.68	63	1.2×10^{-5}
	Ab: y-ATOM^{WDR5} + mCherry Ligand	414.783	135.178	53	7.4×10^{-3}
	Ab: y-ATOM^{SH2} + WDR5 Ligand	840.973	217.723	59	0.96
	Ab: y-ATOM^{SH2} + SH2 Ligand	842.88	194.573	52	-
	Ab: y-ATOM^{SH2} + Ras Ligand	991.333	295.862	52	3.1×10^{-3}
	Ab: y-ATOM^{SH2} + mCherry Ligand	764.598	226.548	39	8.6×10^{-2}
	Ab: y-ATOM^{Ras} + WDR5 Ligand	557.431	170.208	52	0.24
	Ab: y-ATOM^{Ras} + SH2 Ligand	532.763	203.454	55	0.10
	Ab: y-ATOM^{Ras} + Ras Ligand	606.653	243.069	50	-
	Ab: y-ATOM^{Ras} + mCherry Ligand	585.523	181.349	57	0.61
	Ab: y-ATOM^{mCherry} + WDR5 Ligand	503.876	122.081	55	1.8×10^{-2}
	Ab: y-ATOM^{mCherry} + SH2 Ligand	440.289	128.071	53	3.6×10^{-5}
	Ab: y-ATOM^{mCherry} + Ras Ligand	428.388	170.887	52	$5.5 - 10^{-5}$
	Ab: y-ATOM^{mCherry} + mCherry Ligand	580.192	199.945	54	-
	y-ATOM^{WDR5} + WDR5 Ligand	169.115	93.255	55	-
	y-ATOM^{WDR5} + SH2 Ligand	9.872	2.435	62	1.5×10^{-23}
	y-ATOM^{WDR5} + Ras Ligand	10.597	2.185	63	1.8×10^{-23}
	y-ATOM^{WDR5} + mCherry Ligand	8.199	2.253	53	3.2×10^{-23}
	y-ATOM^{SH2} + WDR5 Ligand	89.787	42.767	59	1.9×10^{-25}
	y-ATOM^{SH2} + SH2 Ligand	1559.245	772.165	52	-
	y-ATOM^{SH2} + Ras Ligand	84.582	32.517	52	5.5×10^{-25}
	y-ATOM^{SH2} + mCherry Ligand	137.138	57.964	39	9.9×10^{-23}
	y-ATOM^{Ras} + WDR5 Ligand	22.247	12.501	52	8.5×10^{-18}
	y-ATOM^{Ras} + SH2 Ligand	24.051	12.134	55	8.1×10^{-18}
	y-ATOM^{Ras} + Ras Ligand	351.468	221.633	50	-
	y-ATOM^{Ras} + mCherry Ligand	23.1	10.747	57	5.5×10^{-18}
	y-ATOM^{mCherry} + WDR5 Ligand	51.934	20.425	55	3.0×10^{-23}
	y-ATOM^{mCherry} + SH2 Ligand	38.506	22.964	53	6.1×10^{-24}
	y-ATOM^{mCherry} + Ras Ligand	22.568	17.654	52	6.4×10^{-25}
	y-ATOM^{mCherry} + mCherry Ligand	485.916	248.834	54	-
Extended Data Fig. 2	c-ATOM^{Ras} + WDR5 Ligand	0.064433	0.051485	51	1.3×10^{-15}
	c-ATOM^{Ras} + SH2 Ligand	0.05989	0.034335	43	2.8×10^{-15}
	c-ATOM^{Ras} + hRas Ligand	1.372623	0.852036	40	-
	y-ATOM^{SH2} + WDR5 Ligand	0.431548	0.171098	51	3.0×10^{-25}
	y-ATOM^{SH2} + SH2 Ligand	8.126186	3.506001	43	-
	y-ATOM8^{SH2} + hRas Ligand	0.391623	0.20875	40	4.1×10^{-24}
	r-ATOM^{WDR5} + WDR5 Ligand	4.649199	2.408491	51	-
	r-ATOM^{WDR5} + SH2 Ligand	0.384141	0.191128	43	9.7×10^{-22}
	r-ATOM^{WDR5} + hRas Ligand	0.136863	0.107134	40	5.5×10^{-23}

Figure	Condition	Average	Std. Dev.	n	p value
Extended Data Fig. 3	Ab: y-ATOM^{WDR5} WT	551.020	195.300	61	0.72
	Ab: y-ATOM^{WDR5} R80A	538.706	173.495	55	
	y-ATOM^{WDR5} WT	27.010	12.955	61	2.6×10^{-17}
	y-ATOM^{WDR5} R80A	8.627	5.848	55	
Supp. Fig. S4	y-ATOM^{SH2} + SH2 Ligand	263.708	219.228	63	3.8×10^{-15}
	y-ATOM^{SH2} + mCherry Ligand	11.224	8.107	49	
	y-ATOM^{mCherry} + SH2 Ligand	6.936	1.868	54	1.1×10^{-16}
	y-ATOM^{mCherry} + mCherry Ligand	160.797	120.695	59	
Supp. Fig. S6	MB1^{WDR5}-FP1 + Ligand	0.662	0.382	57	0.43
	MB1^{WDR5}-FP1 − Ligand	0.601	0.411	51	
	MB1^{WDR5}-FP2 + Ligand	0.294	0.172	48	6.4×10^{-6}
	MB1^{WDR5}FP2 − Ligand	0.151	0.114	47	
	MB1^{WDR5}-FP3 + Ligand	0.255	0.16	52	3.8×10^{-16}
	MB1^{WDR5}-FP3 − Ligand	0.036	0.024	49	

Supplementary Material

Refer to Web version on PubMed Central for supplementary material.

Acknowledgements

We thank X. Wang and X.-J. Chen for advice on mitochondrial imaging and for the gift of HEK 293T and HeLa cells, R. Oot and S. Wilkens for the gift of MDA-MB-231 cells, M. Mollapour for the gift of COS-7 cells, M. Cosgrove for the gift of the WDR5 expression plasmid and S. Koide for the gift of the *MB^{SH2}* and *SH2* genes. This work was supported by National Institutes of Health grant nos. F30 GM146428 to H.S. and R01 GM148448 to S.N.L.

Data availability

All raw and processed data, statistical analyses and images (with associated metadata) generated in this work have been deposited to the Figshare repository (https://doi.org/10.58120/upstate.23959239.v2). This work did not generate any code. Plasmids expressing ATOM biosensors have been deposited to Addgene (Addgene codes 209702–209721). All other resources used in this study will be made available upon request.

References

1. Nakai J, Ohkura M & Imoto K A high signal-to-noise Ca^{2+} probe composed of a single green fluorescent protein. Nat. Biotechnol 19, 137–141 (2001). [PubMed: 11175727]
2. Baird GS, Zacharias DA & Tsien RY Circular permutation and receptor insertion within green fluorescent proteins. Proc. Natl Acad. Sci. USA 96, 11241–11246 (1999). [PubMed: 10500161]
3. Nasu Y, Shen Y, Kramer L & Campbell RE Structure- and mechanism-guided design of single fluorescent protein-based biosensors. Nat. Chem. Biol 17, 509–518 (2021). [PubMed: 33558715]
4. van der Linden FH et al. A turquoise fluorescence lifetime-based biosensor for quantitative imaging of intracellular calcium. Nat. Commun 12, 7159 (2021). [PubMed: 34887382]

5. Inoue M. et al. Rational design of a high-affinity, fast, red calcium indicator R-CaMP2. Nat. Methods 12, 64–70 (2015). [PubMed: 25419959]
6. Inoue M. et al. Rational engineering of XCaMPs, a multicolor GECI suite for in vivo imaging of complex brain circuit dynamics. Cell 177, 1346–1360.e24 (2019). [PubMed: 31080068]
7. Sun XR et al. Fast GCaMPs for improved tracking of neuronal activity. Nat. Commun 4, 2170 (2013). [PubMed: 23863808]
8. Chen T-W et al. Ultrasensitive fluorescent proteins for imaging neuronal activity. Nature 499, 295–300 (2013). [PubMed: 23868258]
9. Binz HK, Amstutz P & Plückthun A Engineering novel binding proteins from nonimmunoglobulin domains. Nat. Biotechnol 23, 1257–1268 (2005). [PubMed: 16211069]
10. Koide A, Bailey CW, Huang X & Koide S The fibronectin type III domain as a scaffold for novel binding proteins. J. Mol. Biol 284, 1141–1151 (1998). [PubMed: 9837732]
11. Hamers-Casterman C. et al. Naturally occurring antibodies devoid of light chains. Nature 363, 446–448 (1993). [PubMed: 8502296]
12. Kroning KE et al. A modular fluorescent sensor motif used to detect opioids, protein-protein interactions, and protease activity. ACS Chem. Biol 17, 2212–2220 (2022). [PubMed: 35925780]
13. Stumpp MT, Binz HK & Amstutz P. DARPins: a new generation of protein therapeutics. Drug Discov. Today 13, 695–701 (2008). [PubMed: 18621567]
14. Amstutz P. et al. Intracellular kinase inhibitors selected from combinatorial libraries of designed ankyrin repeat proteins. J. Biol. Chem 280, 24715–24722 (2005). [PubMed: 15851475]
15. Nord K. et al. Binding proteins selected from combinatorial libraries of an α-helical bacterial receptor domain. Nat. Biotechnol 15, 772–777 (1997). [PubMed: 9255793]
16. Lajoie MJ et al. Designed protein logic to target cells with precise combinations of surface antigens. Science 369, 1637–1643 (2020). [PubMed: 32820060]
17. Langan RA et al. De novo design of bioactive protein switches. Nature 572, 205–210 (2019). [PubMed: 31341284]
18. John AM, Sekhon H, Ha J-H & Loh SN Engineering a fluorescent protein color switch using entropy-driven β-strand exchange. ACS Sens. 7, 263–271 (2022). [PubMed: 35006676]
19. Wojcik J. et al. A potent and highly specific FN3 monobody inhibitor of the Abl SH2 domain. Nat. Struct. Mol. Biol 17, 519–527 (2010). [PubMed: 20357770]
20. Gupta A. et al. Facile target validation in an animal model with intracellularly expressed monobodies. Nat. Chem. Biol 14, 895–900 (2018). [PubMed: 30013062]
21. Spencer-Smith R. et al. Inhibition of RAS function through targeting an allosteric regulatory site. Nat. Chem. Biol 13, 62–68 (2017). [PubMed: 27820802]
22. Fridy PC et al. A robust pipeline for rapid production of versatile nanobody repertoires. Nat. Methods 11, 1253–1260 (2014). [PubMed: 25362362]
23. Do K & Boxer SG GFP variants with alternative β-strands and their application as light-driven protease sensors: a tale of two tails. J. Am. Chem. Soc 135, 10226–10229 (2013). [PubMed: 23819615]
24. Tsien RY The green fluorescent protein. Annu. Rev. Biochem 67, 509–544 (1998). [PubMed: 9759496]
25. Balleza E, Kim JM & Cluzel P Systematic characterization of maturation time of fluorescent proteins in living cells. Nat. Methods 15, 47–51 (2018). [PubMed: 29320486]
26. Wang P. et al. WDR5 modulates cell motility and morphology and controls nuclear changes induced by a 3D environment. Proc. Natl Acad. Sci. USA 115, 8581–8586 (2018). [PubMed: 29987046]
27. Sirvent A, Benistant C & Roche S Cytoplasmic signalling by the c-Abl tyrosine kinase in normal and cancer cells. Biol. Cell 100, 617–631 (2008). [PubMed: 18851712]
28. Kim J-H et al. High cleavage efficiency of a 2A peptide derived from porcine teschovirus-1 in human cell lines, zebrafish and mice. PLoS ONE 10.1371/journal.pone.0018556 (2011).
29. Shariati K. et al. A superfolder green fluorescent protein-based biosensor allows monitoring of chloride in the endoplasmic reticulum. ACS Sens. 7, 2218–2224 (2022). [PubMed: 35951356]

30. Oliinyk OS et al. Single-domain near-infrared protein provides a scaffold for antigen-dependent fluorescent nanobodies. Nat. Methods 19, 740–750 (2022). [PubMed: 35606446]
31. Tang JC et al. Detection and manipulation of live antigen-expressing cells using conditionally stable nanobodies. eLife 5, e15312 (2016). [PubMed: 27205882]
32. Feng J. et al. A general strategy to construct small molecule biosensors in eukaryotes. eLife 4, e10606 (2015). [PubMed: 26714111]
33. Navarro R, Chen L, Rakhit R & Wandless TJ A novel destabilizing domain based on a small-molecule dependent fluorophore. ACS Chem. Biol 11, 2101–2104 (2016). [PubMed: 27243964]
34. Sekhon H, Ha J-H & Loh SN Enhancing response of a protein conformational switch by using two disordered ligand binding domains. Front. Mol. Biosci 10, 1114756 (2023). [PubMed: 36936990]
35. Zheng H, Bi J, Krendel M & Loh SN Converting a binding protein into a biosensing conformational switch using protein fragment exchange. Biochemistry 53, 5505–5514 (2014). [PubMed: 25084233]
36. Dingus JG, Tang JC, Amamoto R, Wallick GK & Cepko CL A general approach for stabilizing nanobodies for intracellular expression. eLife 11, e68253 (2022). [PubMed: 36416528]
37. Nasu Y. et al. A genetically encoded fluorescent biosensor for extracellular L-lactate. Nat. Commun 12, 7058 (2021). [PubMed: 34873165]
38. Wu S-Y et al. A sensitive and specific genetically-encoded potassium ion biosensor for in vivo applications across the tree of life. PLoS Biol. 20, e3001772 (2022). [PubMed: 36067248]
39. Blanden AR et al. Zinc shapes the folding landscape of p53 and establishes a pathway for reactivating structurally diverse cancer mutants. eLife 9, e61487 (2020). [PubMed: 33263541]
40. Schindelin J. et al. Fiji: an open-source platform for biological-image analysis. Nat. Methods 9, 676–682 (2012). [PubMed: 22743772]

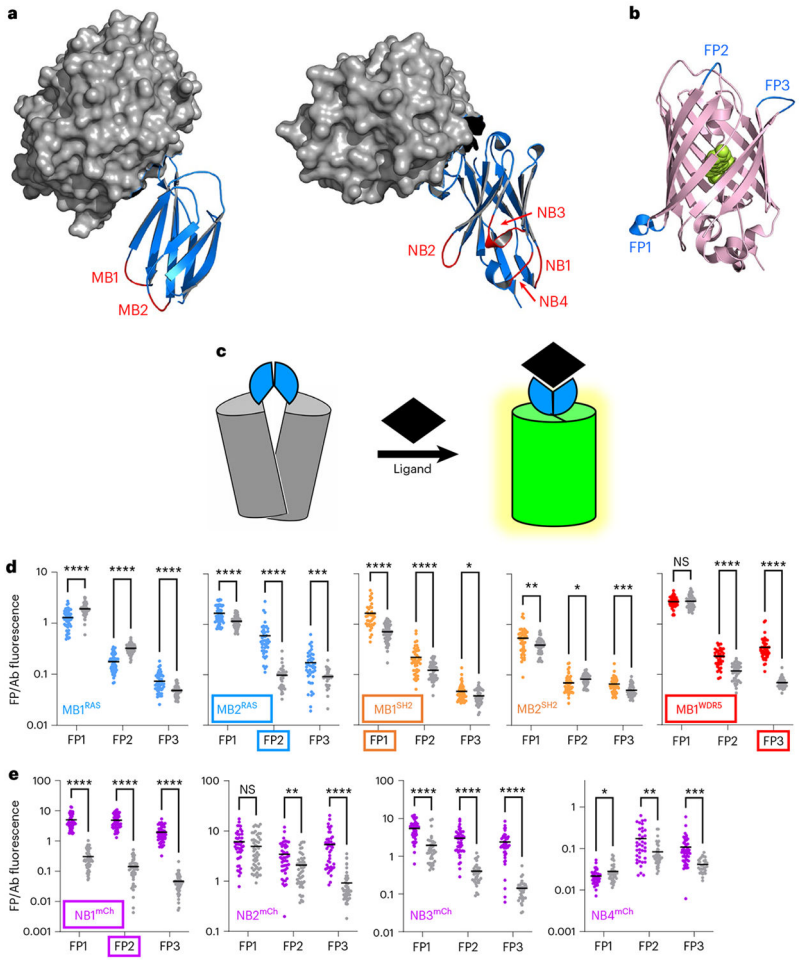

Fig. 1 |. Biosensor design and screening y-ATOM sensors in HEK 293T cells.

a, X-ray structures of MB^{WDR5} (blue structure at left) and NB^{mCh} (blue structure to the right) are shown bound to WDR5 and mCh (gray structures), respectively. MB and NB domains were circularly permuted at loops MB1–MB2 and NB1–NB4 (red), respectively (Protein Data Bank 6BYN and 8IM0). **b**, MB and NB permutants were inserted into YFP (pink) at one of the three loops depicted in blue (FP1–FP3). The YFP chromophore is shown in green spheres (Protein Data Bank 5WJ2). **c**, In the proposed turn-on mechanism, the MB or NB domain (blue) is partially unfolded in the absence of ligand (black), which disrupts the conformation of the FP domain (cylinder), leaving the chromophore in an unmatured state. Ligand binding induces the MB–NB domain to fold, restoring the native conformation of the FP and allowing the chromophore to mature. **d**,**e**, Fluorescence turn-on of MB-based y-ATOM sensors (**d**) and NB-based y-ATOM sensors (**e**) was determined in HEK 293T cells, with the best-performing combination of MB/NB and FP domains indicated by the colored boxes. Cognate and noncognate ligands for each sensor are designated by colored and gray symbols, respectively. Ab on the *y* axes denotes fluorescence intensity of the anti-GFP antibody used to measure total biosensor expression. Each data point represents a cell. $****P < 10^{-4}$, $***P < 10^{-3}$, $**P < 10^{-2}$, $*P < 0.05$; NS, not significant. Number of cells, means, standard deviations (s.d.) and *P* values obtained by a two-tailed t-test for all

valid comparisons are included in Extended Data Table 1. The results are representative of at least three BRs. See Supplementary Figs. 1-3 and 8 for cell images.

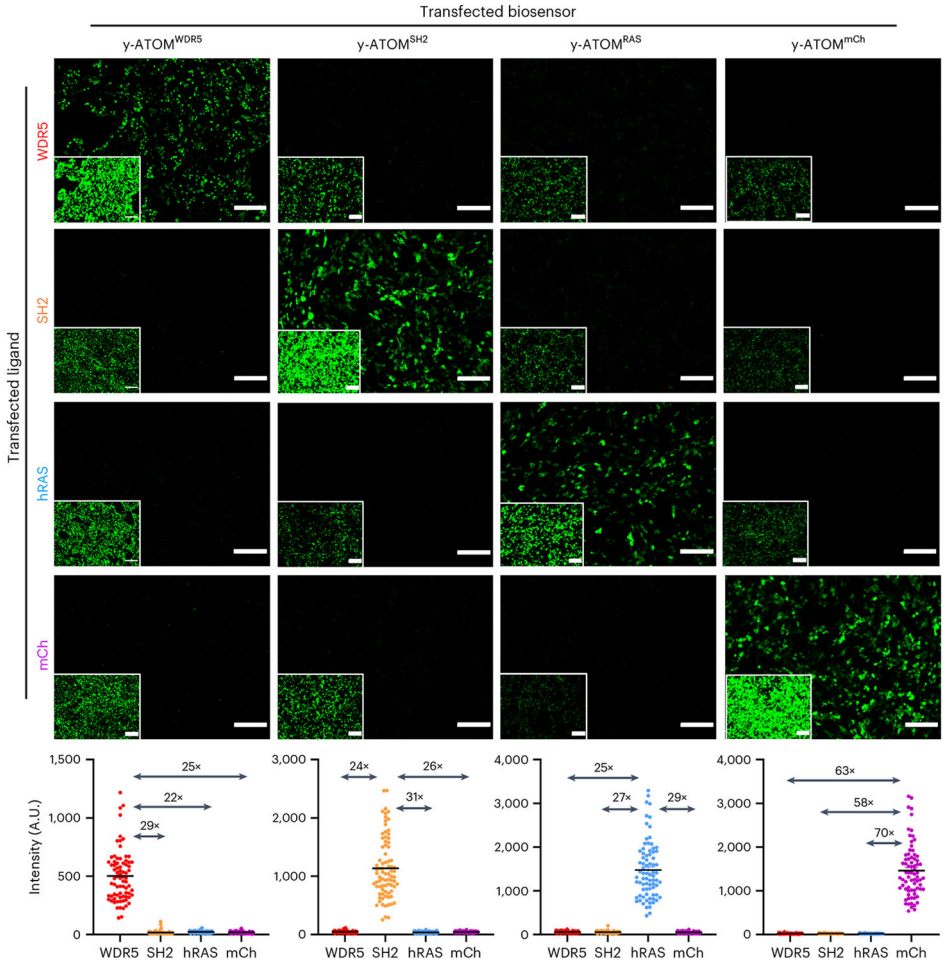

Fig. 2 |. y-ATOM sensors show high selectivity and fluorescence turn-on in human cells.
Images on the diagonal represent cells transfected with plasmids expressing biosensor and cognate ligand. The off-diagonal images are cells transfected with plasmids expressing biosensor and decoy ligands. Higher contrast settings are shown in the insets to demonstrate that biosensors were expressed (but dim) in the off-diagonal cells. Fluorescence turn-on is quantified at the bottom. Each data point represents a cell. $P < 10^{-4}$ for all comparisons shown. Scale bars, 200 μm. The results are representative of four BR. Number of cells, means, s.d. and *P* values obtained by a two-tailed *t*-test for all valid comparisons are included in Extended Data Table 1. A.U., arbitrary units.

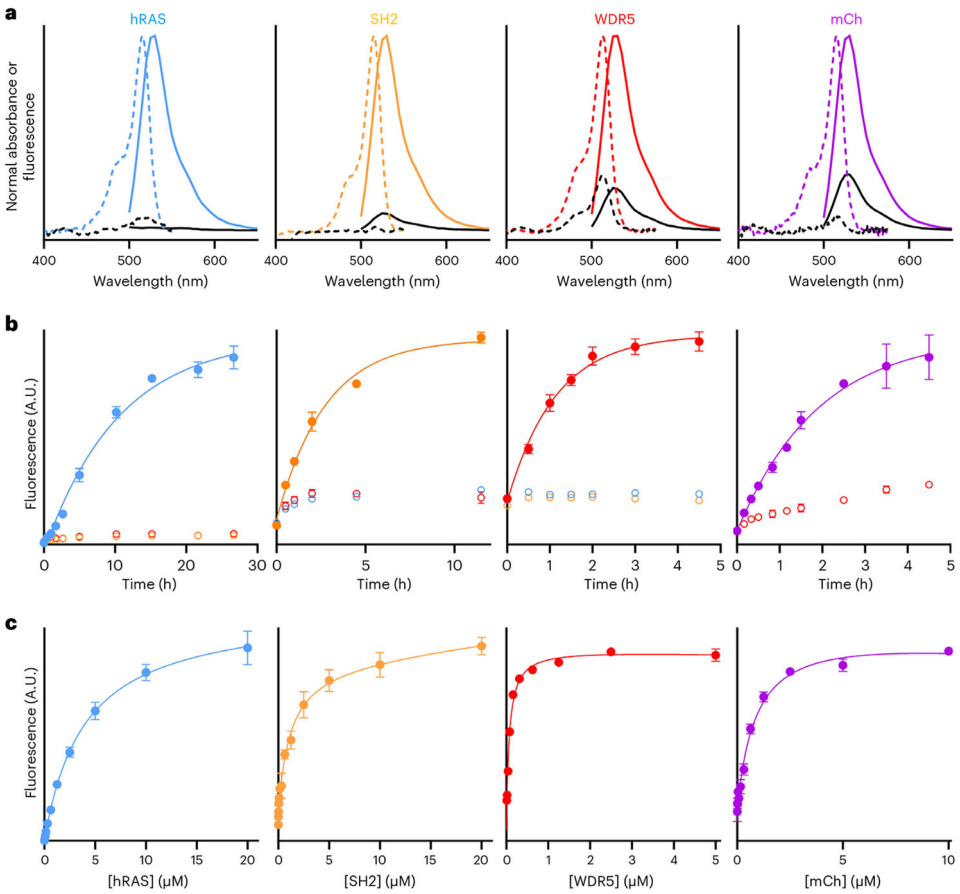

Fig. 3 |. Characterization of purified y-ATOM sensors at 37 °C.

Sensors and ligands are colored cyan (hRAS), orange (SH2), red (WDR5) and purple (mCh). **a**, Fluorescence turn-on resulted from ligand-induced chromophore maturation, as evidenced by the increase in absorbance at 514 nm (dashed lines) and fluorescence at 530 nm (solid lines). Samples contained 10 μM ligand. Data were recorded at time zero (black lines) and 12 h (colored lines). **b**, Fluorescence was activated in a ligand-specific manner with half-times of 1.7–7.4 h. Lines are best fits of the data to a single exponential function. Filled and empty circles represent cognate and decoy ligands, respectively. **c**, y-ATOM sensors bound their cognate targets with low nM to low μM K_d. Lines are best fits of the data to the one-site binding equation. Data are plotted as mean ± s.d. (n = 3 technical repeats, defined as data obtained from the same stock of purified protein; data are representative of two to three BRs). A.U., arbitrary units. Fitted values are reported in Table 1.

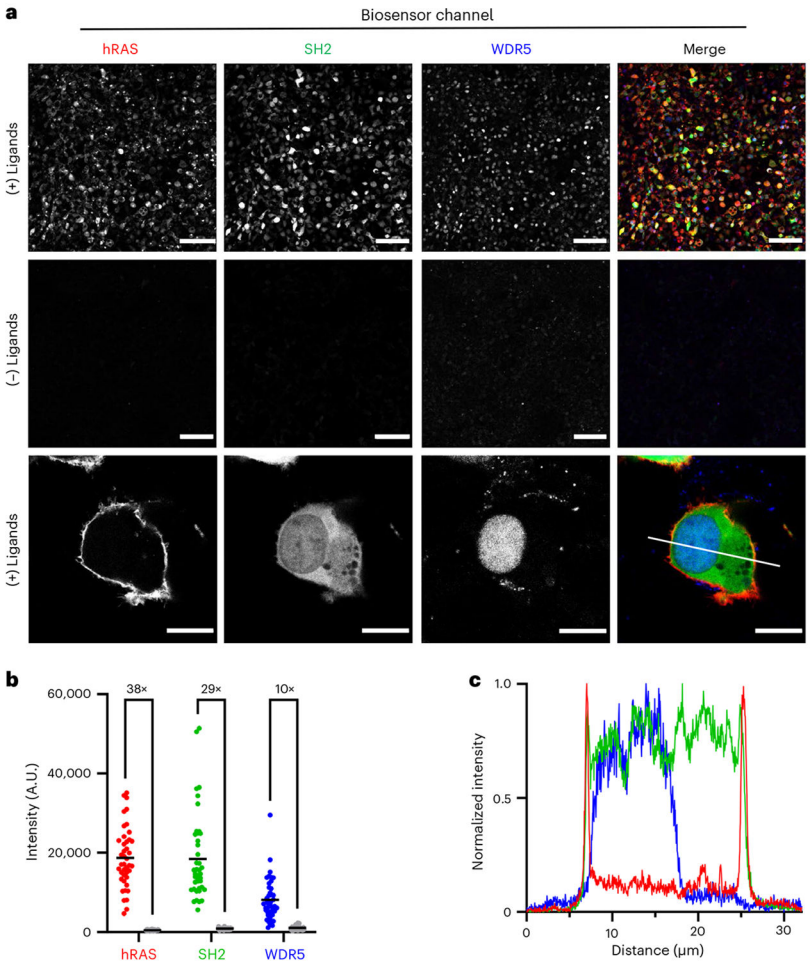

Fig. 4 |. Multiplexed three-color imaging shows ATOM sensors detect subcellular localization of protein targets.

For visual clarity, the cyan channel (hRAS) is pseudocolored red, the yellow channel (SH2) is pseudocolored green and the red channel (WDR5) is pseudocolored blue. **a**, Cells cotransfected with a mixture of c-ATOM^{RAS}, y-ATOM^{SH2} and r-ATOM^{WDR5} expressing plasmids, and a fourth plasmid encoding all three ligands showed fluorescence turn-on specific to the presence of ligands (top row and middle row). The higher contrast settings in the insets demonstrated that biosensors expressed but were dim. Focusing on a single cell (bottom row) revealed distinct biosensor fluorescence localized to the plasma membrane (c-ATOM^{RAS}), cytoplasm (y-ATOM^{SH2}) and (r-ATOM^{WDR5}). Scale bars are 100 μm in top and middle rows, and 10 μm in the bottom row. **b**, Sensor turn-on was calculated by dividing the average intensity of the cells in the top row of **a** (red circles) by that of the cells in the middle row of **a** (gray circles). Each data point represents a cell (42 per experiment). **P** < 10^{-4} for all comparisons shown. The results are representative of four BRs. **c**, A line trace through the cell shown in the bottom row of **a** confirmed the expected locations of hRAS, SH2 and WDR5 in the plasma membrane (red trace), cytoplasm (green trace) and nucleus (blue trace), respectively. Number of cells, means, s.d. and **P** values obtained by a two-tailed *t*-test for all valid comparisons are included in Extended Data Table 1

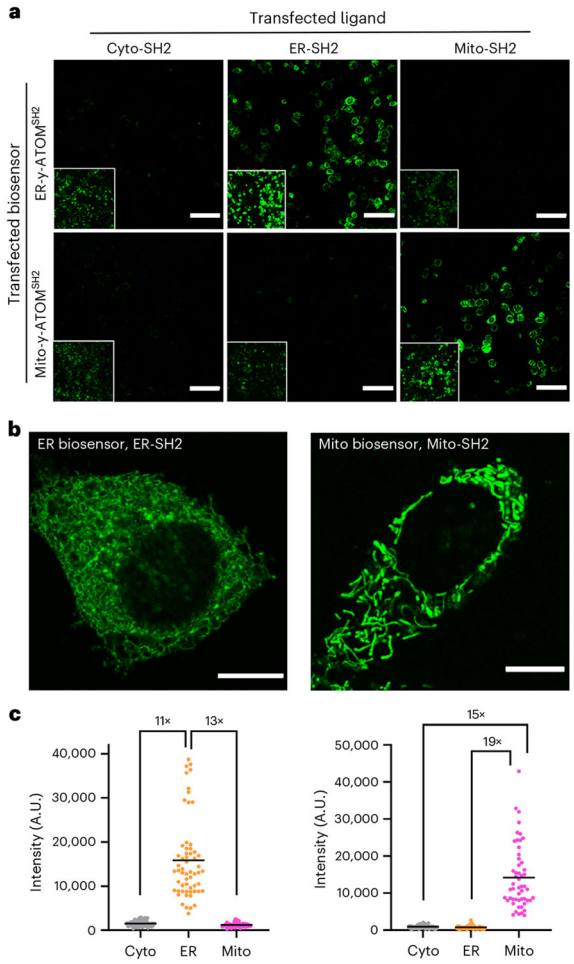

Fig. 5 |. y-ATOM^{SH2} can function as an ER- or mitochondria-targeted biosensor.
a, HeLa cells transfected with ER-localized biosensor (top row) or mito-localized biosensor (bottom row) were activated specifically by ER-localized SH2 and mito-localized SH2, respectively, and not by SH2 which targeted other compartments. Insets show higher contrast settings to demonstrate that biosensors were expressed in all transfection conditions. Scale bars, 100 μm. **b**, Confocal images confirmed that the biosensors were detecting their targets in the expected organelles. Scale bars, 10 μm. **c**, Quantification of the data in **a** found 11–13-fold selective turn-on for ER-targeted sensor and ligand, and 15–19-fold selective turn-on for mito-targeted sensor and ligand. Each data point represents a cell (52–63 per experiment). $P < 10^{-4}$ for all comparisons shown. The results are representative of three BRs. Number of cells, means, s.d. and P values obtained by a two-tailed t-test for all valid comparisons are included in Extended Data Table 1.

Table 1 |

Properties of ATOM sensors

Sensor	Binding domain	FP domain	Fold turn-on in cells[a]	Fold turn-on in vitro	K_d (μM)	k_{on} (h^{-1})
y-ATOM^{RAS}	MB2^{RAS}	YFP FP2	22.9±4.4	>100	3.96±0.29	0.094±0.0.0096
y-ATOM^{SH2}	MB1^{SH2}	YFP FP1	21.9±4.5	8.3	1.62±0.21	0.38±0.023
y-ATOM^{WDR5}	MB1^{WDR5}	YFP FP3	24.0±3.2	4.9	0.0188±0.0052	0.49±0.12
c-ATOM^{RAS}	MB2^{RAS}	mTurquoise FP2	17.4±4.2	ND	ND	ND
r-ATOM^{WDR5}	MB1^{wDR5}	mTagRFP FP3	15.7±6.3	ND	ND	ND
y-ATOM^{mCh}	NB1^{mCh}	YFP FP2	62.1±14	21	0.776±0.096	0.39±0.12

[a]Calculated by dividing the fluorescence of cells expressing cognate ligand by fluorescence of cells expressing the three noncognate ligands (as shown in Fig. 2), averaged over three BRs. Errors are s.d. (n=3 BRs); ND, not determined.